Fabrication of Sb2S3 thin films by magnetron sputtering and post-sulfurization/selenization for substrate structured solar cells

J. Luo, W. Xiong, G. Liang, Y. Liu, H. Yang, Z. Zheng, Xianghua Zhang, P. Fan, S. Chen

Fabrication of Sb_2S_3 thin films by magnetron sputtering and post-sulfurization/selenization for substrate structured solar cells

Jingting Luo,[a,#] Wei Xiong,[a] Guangxing Liang,[a,#] Yike Liu,[b] Haozhi Yang,[a] Zhuanghao Zheng,[a] Xianghua Zhang,[c] Ping Fan,[a] Shuo Chen[a,*]

[a]*Shenzhen Key Laboratory of Advanced Thin Films and Applications, College of Materials Science and Engineering, College of Physics and Optoelectronic Engineering, Shenzhen University, Shenzhen, 518060, China*

[b]*School of Material and Metallurgical Engineering, Guizhou Institute of Technology, Guiyang 550003, China*

[c]*Univ Rennes, CNRS, ISCR (Institut des Sciences Chimiques de Rennes) UMR 6226, F-35000 Rennes, France*

[*]Corresponding author: Email: chensh@szu.edu.cn (Prof. Chen)

[#]Jingting Luo and Guangxing Liang contributed equally

ABSTRACT: Antimony sulphide (Sb_2S_3) as an environment-friendly and cost-efficiently photovoltaic material has drawn tremendous research attentions. To broaden its scope of applications as flexible or tandem devices, Sb_2S_3 solar cells with substrate structure that are rarely reported and really need further exploration. In this work, an efficient method of magnetron sputtering using Sb_2S_3 target followed with post-sulfurization or post-selenization heat treatment process has been used to prepare S-Sb_2S_3 and Se-Sb_2S_3 thin films, then substrate structured Sb_2S_3 solar cells with configuration of Mo/Sb_2S_3/CdS/ITO/Ag were fabricated. The solar cell based on crystalline S-Sb_2S_3 thin film can achieve power conversion efficiency (PCE) of 0.49%.

In contrast, a post-selenization treatment can induce the formation of $Sb_2(S,Se)_3$ ternary phase and obtain high-quality thin film with uniform granular crystals. The corresponding substrate structured thin film solar cell shows a significant two times improvement of PCE to 0.95%, also with an increased external quantum efficiency (EQE) value and an extended response region, which can be attributed to the Se-Sb_2S_3 thin films with lower band gap, better crystallinity and less recombination loss. The combined features of advantageous vacuum preparation process and efficient substrate device structure further demonstrated its attractive application potential in thin film photovoltaic scenarios.

KEYWORDS: Sb_2S_3, magnetron sputtering, post-sulfurization/post-selenization, substrate structure, thin film solar cells

1. Introduction

With the increasing demand of sustainable and effective sources of energy to partially compensate the non-renewable fossil fuels, the solar energy has drawn tremendous research attentions thanks to its great application potential.[1-3] Among the widely application fields, solar cells can directly absorb the incident sunlight to generate electric power, and the continuous exploring effective photovoltaic materials to improve the power conversion efficiency (PCE) is one of the main concern.[4,5] Recently, the inorganic compound thin film solar cells have achieved a rapid development due to their advantages of low material consumption, low energy consumption, high temperature power generation performance and the flexibility.[6-10]

Among them, cadmium telluride (CdTe) and copper indium gallium selenide (CIGS) solar cells with impressive PCEs higher than 22% are two of the most representative thin film solar cells.[11] However, the intrinsic toxicity of Cd, the natural scarcity of Te, In and Ga still limit their broader scope of applications. Thus some alternative environment-friendly and cost-efficiently photovoltaic materials are actively investigated. Antimony sulfide (Sb_2S_3) with non-toxic, low-cost and earth-abundant constitutes has emerged as a promising candidate. Additionally, Sb_2S_3 shows excellent optoelectronic properties, such as an appropriate band gap (~1.7 eV), large absorption coefficient (>10^5 cm^{-1}) and an ideal match in highly efficient Si-based tandem dual-junction solar cells with theoretical PCE exceeding 40%.[2,8,12-14]

State-of-the-art Sb_2S_3 solar cells have achieved record PCEs of 7.50% and 6.56% for mesoporous sensitized and planar geometries, respectively.[13,15] The planar device structure is considered as a more appropriate design for Sb_2S_3 thin film solar cells to gain expected efficiency, and a significant progress can be observed in the last decade.[2,4] As for the Sb_2S_3 planar heterojunction solar cells, there are also two different scenarios, including superstrate and substrate cell structures. Up to now, almost all the works are focused on the superstrate structure due to its simple preparation process and an ohmic contact for Sb_2S_3 absorber layer.[8,16-18] Only a few studies to fabricate substrate structured Sb_2S_3 thin film solar cells have been reported. For example, Zhang et al. prepared Sb_2S_3 thin film by evaporating metallic Sb particles followed with annealing in N_2/H_2S environment, a Sb_2S_3 solar cell with substrate structure of Mo/Sb_2S_3/CdS/i-ZO/AZO/Ni:Al has achieved a PCE of

0.65%.[19] Pan et al. used rapid thermal evaporation method to deposit Sb_2S_3 thin film on Mo substrate and then fabricated a similar substrate structured Sb_2S_3 thin film solar cell with an interesting efficiency of 1.75%, which is the best PCE belonging to this substrate configuration by now.[20] Therefore, it needs further exploration of the substrate structured Sb_2S_3 thin film solar cells in order to broaden its applications on flexible or tandem solar cells.

Sb_2S_3 thin films can be prepared by various methods such as chemical bath deposition,[21] solution processing,[22] fast chemical approach,[23] atomic layer deposition,[24] hydrothermal,[25] thermal (or rapid thermal) evaporation[8,26] and the magnetron sputtering.[27] Among these methods, the widely used ones for preparing planar Sb_2S_3 solar cells are the chemical bath deposition and the thermal evaporation. However, the attached shortcomings, e.g., time consuming and inevitable introduction of impurities for the former method, source wasting and easy deviation of the stoichiometric ratio for the other method, which might affect its practical applications. In contrast, magnetron sputtering is a promising full-vacuum technique with some advantages like accurate composition transfer from targets to films, good uniformity over large areas and competitive industrial scale-up.[27,28] In this work, the amorphous Sb_2S_3 thin film was firstly deposited by Radio Frequency (RF) magnetron sputtering, and then an additional post-sulfurization or post-selenization heat treatment was applied to obtain high-quality crystalline Sb_2S_3 thin film. Sb_2S_3 solar cells with substrate structure of Mo/Sb_2S_3/CdS/ITO/Ag have achieved interesting PCEs of 0.49% and 0.95% for post-sulfurization and post-selenization involved process,

respectively. The combined features of effective device structure and advantageous preparation process further demonstrated its attractive potential for thin film photovoltaic applications.

2. Experimental details

2.1. Preparation of Sb_2S_3 thin film solar cells

An effective RF magnetron sputtering using a high-purity Sb_2S_3 target followed with post-sulfurization or post-selenization treatment was applied to prepare Sb_2S_3 thin films. A schematic illustration of the preparation process is shown in Fig. 1. Mo-coated soda lime glass was chosen as device substrate, prior to sputtering, it was ultrasonically cleaned in sequential detergent, acetone, isopropanol and ethanol solution for 10 min, respectively. The sputtering system has 2-in magnetron sputtering guns and a rotatable substrate holder. The deposition chamber was evacuated to a residual pressure of less than 7.6×10^{-4} Pa before each deposition. Argon gas was introduced at a rate of 20 sccm and the deposition was carried out with a fixed power of 35 W also with a relatively low deposition pressure of 0.5 Pa to ensure a high compactness. The deposition time of the Sb_2S_3 thin film was 90 min and the obtained thickness was about 900 nm. After that, an additional post-sulfurization or post-selenization heat treatment was applied in order to release the internal stress of the as-deposited thin film, to eliminate the possible detrimental sulfur vacancies and to obtain highly crystalline Sb_2S_3 thin films. In detail, high purity S powder (99.999%) or Se power (99.999%) and the as-deposited thin film were placed into a double-chamber vacuum tubular furnace, respectively. The post-sulfurization was

carried out at different temperatures (200 ℃, 300 ℃, 400 ℃, 425 ℃, 450 ℃ and 475 ℃) for 20 min, and the samples were denoted as S-Sb_2S_3 thin films. Differently, the post-selenization process was last for 5 min at temperatures of 350 ℃, 375 ℃, 400 ℃ and 425 ℃, these samples were denoted as Se-Sb_2S_3 thin films.

After the deposition of Sb_2S_3 thin film with p-type conductivity as confirmed by a Semilab PN-100 tester, the n-type CdS buffer layer was then deposited onto the absorber layer via chemical bath deposition method (Fig. 1c). An additional heat treatment at 300 ℃ for 10 min was used to induce elemental inter-diffusion and optimize the band alignment. Indium tin oxide (ITO) window layer was subsequently deposited using magnetron sputtering at room temperature. Finally, the device surface was scribed into small squares with identical area and then Ag colloids were painted onto the surface to form metallic contact, the effective device area was fixed to 0.135 cm^2 (Fig. 1d). Sb_2S_3 thin film solar cell with substrate structure of Mo/Sb_2S_3/CdS/ITO/Ag was prepared and used for the subsequent performance measurements.

2.2 Characterizations

The crystal structure of Sb_2S_3 thin films were characterized by X-ray diffraction (XRD, Ultima-iv) with CuK_α radiation under operation conditions of 40 kV and 40 mA. Morphologies of the Sb_2S_3 thin films were obtained from a Zeiss SUPRA 55 thermal field emission scanning electron microscope (SEM). The chemical compositions and the corresponding elemental mappings were analyzed by SEM-coupled Energy Dispersive X-ray Spectroscope (EDS, BRUKER QUANTAX

200). A Shimadzu UV-3600 UV/Vis/NIR spectrophotometer equipped with monochromator was used for the optical reflectance and transmittance investigation, herein, pure soda-lime glass was chosen as the substrate for the Sb_2S_3 thin film deposition and the post-sulfurization was carried out at 200 ℃, 300 ℃ and 400 ℃. Current density-voltage (J-V) curves were measured by using a multi-meter (Keithley, 2000 Series) under AM 1.5G light illumination from a 3A solar simulator with intensity calibrated to 100 mW/cm^2 through a Si reference cell. The voltage was forwardly and backwardly scanned from -0.1 V to 0.6 V with a scan rate of 0.02 V/s. The external quantum efficiency (EQE) spectra were obtained using a Zolix SCS101 system with a monochromator and a Keithley 2400 source meter.

3. Results and discussion

3.1 S-Sb_2S_3 thin films and the device performances

Fig. 2a shows the XRD patterns of the as-deposited and post-sulfurized S-Sb_2S_3 thin films at different temperatures. No diffraction peaks correspond to the crystalline phase can be observed except a single peak originated from Mo substrate (2θ=41°), implying the amorphous nature of the as-deposited thin film. Afterwards, the thin film was annealed under sulfur atmosphere (post-sulfurization) at six temperatures of 200 °C, 300 °C, 400 °C, 425 °C, 450 °C and 475 °C, respectively. No crystalline Sb_2S_3 phase can be detected when the post-sulfurization temperature below 200 °C. Then undergo post-sulfurization higher than 300 °C, all the emerging peaks of the thin films are in good agreement with the JCPDS card (No. 42-1393) of the orthorhombic phase of Sb_2S_3 without a second phase. The sharp diffraction peaks also indicate the

highly crystalline nature of these S-Sb_2S_3 thin films. In order to study the thin film orientation, texture coefficients (TC) of the diffraction peaks were calculated based on the following equation:

$$TC_{hkl} = \frac{I(hkl)}{I_0(hkl)} / (\frac{1}{N} \sum_1^n \frac{I(h_i k_i l_i)}{I_0(h_i k_i l_i)})$$

(1)

where $I_{(hkl)}$ and $I_{0(hkl)}$ are the diffraction peak intensities of (hkl) planes obtained from the measured and standard XRD pattern of Sb_2S_3, respectively.[29] Larger TC value of a diffraction peak indicates a preferential orientation along this particular direction. As shown in Fig. 2b, further increasing the post-sulfurization temperature to 425 °C, an obvious increase of $TC_{(211)}$ value can be observed, suggesting the crystal grains start to grow in vertical direction on the substrate, which is beneficial for reducing interface recombination and absorber transport loss.[30] The elemental composition and the corresponding atomic ratio of Sb/S for the S-Sb_2S_3 thin films are also shown in Fig. 2b. As the post-sulfurization temperature was increased, the ratio of Sb/S is found to first decrease and then increase, implying the as-deposited amorphous thin film is S poor and it is reasonable to occur due to its high vapor pressure. An additional post-sulfurization heat treatment at appropriate temperature can effectively compensate the S loss originated from magnetron sputtering process. Thus the S-Sb_2S_3 thin films post-sulfurized at 425 °C and 450 °C have more precise ratios that close to the standard stoichiometric ratio of 0.67 for Sb_2S_3. However, if the temperature is too high, e.g., 475 °C, a severe stoichiometric deviation can be attributed to the break of compact Sb_2S_3 thin film. Fig. 2c-h present the SEM images

of the as-deposited thin film and the S-Sb_2S_3 thin films post-sulfurized at different temperatures. For the as-deposited amorphous thin film and the 200 °C post-sulfurized thin film, no obvious crystal grains can be observed, which are consistent with the XRD results. After post-sulfurization at 300 °C, large crystal clusters accompanied by boundaries begin to appear, indicating the start of crystal growth, these phenomena become more obvious at 400 °C. When the post-sulfurization temperature is increased to 425 °C, well-shaped Sb_2S_3 crystal grains with clear grain boundaries can be obtained, a preferential growth orientation is also consistent with the XRD results. Further increasing the temperature to 450 °C, it leads to a more dense thin film with more micro-sized crystals, which are Sb_2S_3 crystals fulfill its stoichiometric ratio according to the EDS analysis. However, if the temperature is too high (475 °C), as shown in Fig. 2h, the compact and continuous thin film will be broken, resulting in obvious holes on the surface, therefore, it is crucial to control the post-sulfurization temperature to obtain high-quality Sb_2S_3 absorber layer.

To investigate the optical properties as well as the band gap of the Sb_2S_3 thin films, UV/Vis/NIR spectrophotometer was performed to obtain the reflection and transmission spectra of the as-prepared thin films using glass as substrate and covering a range from 300 nm to 1100 nm. As shown in Fig. 3a, the reflectance of the amorphous thin film is obviously lower than that of the crystalline thin films in the short wavelength absorption region, which is closely related to its density-dependent lower refractive index as well as a different chemical composition under amorphous

state. The transmission spectra (Fig. 3b) also shows a significant red-shift of the short wavelength cut-off edge from 580 nm for the amorphous thin film to about 650 nm for the crystalline thin film. To further understand and engineer its band structure, the band gap of the S-Sb_2S_3 thin films has been calculated according to the following formulas:

$$\alpha = \frac{1}{d}\ln\left(\frac{1-R(\lambda)}{T(\lambda)}\right) \quad (2)$$

$$\alpha hv = C(hv - E_g)^n \quad (3)$$

Where α is the absorption coefficient, d is thickness, R and T are the reflectance and transmittance, respectively.[31] The latter is a typical Tauc formula, where C is a constant, h is the Planck's constant, v is the photon frequency, n is an index defined by 0.5 for direct and 2.0 for indirect bandgap semiconductor.[27] As shown in Fig. 3c, the as-deposited amorphous thin film has a direct band gap E_g of 1.88 eV, then the value decreases to about 1.73 eV for the highly crystalline thin film due to composition and structure evolution. The obtained E_g of 1.73 eV agrees well with the value given in prior publications for crystalline Sb_2S_3.[27] Importantly, this band gap is also appropriate for applications as absorbers in the thin film or Si-based tandem solar cells.

The solar cells with substrate configuration have many advantages, such as tailoring the absorber layer independently, engineering the interface efficiently, and fabricating flexible or tandem solar cells possibly.[20] Herein, Sb_2S_3 thin film solar cell with substrate structure of Mo/Sb_2S_3/CdS/ITO/Ag was prepared and a schematic illustration of this device is shown in Fig. 4a. The representative cross-sectional SEM

image of the device (Fig. 4b) displays obvious layered structure with approximate thickness of 1040 nm, 80 nm and 580 nm for Sb_2S_3, CdS and ITO layer, respectively. The interface between Sb_2S_3 and CdS also shows uniform, compact, well-adherent and pinhole-free characteristics, which is beneficial for reducing charge carrier recombination and current leakage. In addition, compositional spatial distribution was determined by EDS elemental mappings marked with Sb, S, Cd and In, corresponding to the dashed rectangle area in Fig. 4b. Elements of Sb and S with good uniformity throughout the Sb_2S_3 absorber layer can be observed, implying the high quality of this S-Sb_2S_3 thin film post-sulfurized at 450 °C. The elemental mapping results also show observable elemental inter-diffusion, especially for Cd, which can be explained by the additional post-annealing of the device, such manipulation has been reported to be essential for obtaining favorable band alignment and reducing the recombination at the heterojunction interfaces.[7]

Fig. 5 shows the device performances based on the S-Sb_2S_3 thin film post-sulfurized at 450 °C. According the current density-voltage (J-V) curve (Fig. 5a), under the simulated AM1.5G solar irradiation, the device offers a short-circuit current density (J_{SC}) of 3.58 mA/cm^2, an open circuit voltage (V_{OC}) of 442 mV, and a fill factor (FF) of 30.89%, thus achieving a power conversion efficiency of 0.49%. In addition, no obvious hysteresis between forward (J_{SC} to V_{OC}) and backward (V_{OC} to J_{SC}) scans can be observed in our device, suggesting the high-quality S-Sb_2S_3 thin film materials and the reasonable substrate device structure. External quantum efficiency (EQE) spectrum reveals the photoresponse covering the whole visible range, the

maximum value is lower than 30%, indicating the existence of severe interface defects, which still needs defects passivation and junction optimization.[32] The integrated J_{SC} calculated from EQE data is also drawn in Fig. 5b, a value of 3.10 mA/cm^2 is comparable to the J-V measurement result.

3.2 Se-Sb_2S_3 thin films and the device performances

It has been reported that a post-selenization treatment can greatly improve the crystallinity of Sb_2S_3 thin film and pull down its band gap value by partially substituting S with Se.[33] The formation of $Sb_2(S,Se)_3$ alloy can passivate the interface and bulk defects simultaneously, improve the Sb_2S_3/CdS heterojunction quality and enhance the long-wavelength photon quantum yield.[34] Herein, a short time post-selenization heat treatment of the as-deposited Sb_2S_3 thin film is expected to suppress the recombination loss and improve the device performance. Fig. 6a shows the XRD patterns of the as-deposited and post-selenized Se-Sb_2S_3 thin films. The as-deposited thin film still presents amorphous nature. After post-selenization at temperatures of 350 ℃, 375 ℃, 400 ℃ and 425 ℃ for 5 min, all the thin films exhibit prominent peaks correspond to the orthorhombic phase of Sb_2S_3 (JCPDS, No. 42-1393) or Sb_2Se_3 (JCPDS, No. 15-0861), an observable peak shift to the intermediate position suggesting the formation of ternary $Sb_2(S,Se)_3$ crystalline phase after post-selenization. Fig. 6b shows the atomic ratio of Sb/(S+Se) and S/Se. As expected to passivate the sulfur vacancy, all the Sb/(S+Se) ratios are lower than that of the as-deposited Sb_2S_3 amorphous thin film with a value of 0.76. Temperature-induced Sb/(S+Se) ratio variation further confirms an appropriate

temperature is essential to obtain stoichiometric thin film. An obvious increase and then decrease of the S/Se ratio with increasing the post-selenization temperature can also be observed in Fig. 6b. It can be explained by the combined action of Se vapor diffusion in the tube and substitution of S atoms by Se atoms in the precursor Sb_2S_3 thin film. When the post-selenization temperature increased to 400 ℃, equals to the fixed temperature of Se source, a relative equilibrium of thermodynamic and kinetic processes can be achieved, resulting in a maximum value of S/Se ratio. However, if the temperature is too high, e.g., 425 °C, the break of compact Se-Sb_2S_3 thin film will also cause a severe stoichiometric deviation and a sharp decline of pristine S content.

SEM images of the Se-Sb_2S_3 thin films with different post-selenization temperatures are shown in Fig. 7. All the thin films show granular crystals with clear grain boundaries, implying a more superior crystal growth compared to the S-Sb_2S_3 thin films, which is also beneficial for the device performance improvement. After post-selenization at 350 °C for 5 min, some pinholes can be observed on the surface due to an insufficient temperature and time for crystal growth. When the temperature is increased to 375 ℃, as shown in Fig. 7b, the thin film becomes compact with no obvious pinholes. Further increasing the post-selenization temperature, it leads to a more dense and uniform crystalline thin film with an enlarged average grain size of about 400 nm, which is advantageous for suppress the recombination loss at the grain boundaries. As shown in Fig. 7d, the thin film post-selenized at 425 °C has severe break with isolate large crystal grains and is consistent with the XRD analysis.

Accordingly, Mo/Se-Sb_2S_3/CdS/ITO/Ag substrate structured thin film solar cell has

been fabricated, the optimal device performance based on the Se-Sb_2S_3 thin film post-selenized at 400 °C is shown in Fig. 8. The J-V curve under forward scan (Fig. 8a) gives a J_{SC} of 10.33 mA/cm^2, V_{OC} of 301 mV and FF of 30.84%, thus achieving an interesting PCE of 0.95%, which is almost two times higher than the PCE of S-Sb_2S_3 device. Such significant improvement mainly thanks to a near three times enhancement of J_{SC} from 3.58 mA/cm^2 to 10.33 mA/cm^2, and it can be really attributed to the formation of high-quality $Sb_2(S,Se)_3$ absorber thin film with better crystallinity, passivated surface and less recombination loss. Moreover, no obvious hysteresis between forward and backward scans can be observed in this Se-Sb_2S_3 device, further confirming the superior absorber thin film. EQE spectrum (Fig. 8b) shows an increased EQE value and an extended response region (up to ~1000 nm) compared to that of S-Sb_2S_3 device, demonstrating the band gap of Sb_2S_3 has been pulled down after post-selenization treatment. The observable sharp drop of EQE value at long wavelength range is partially because of the incomplete absorption of infrared photons and the incomplete collection of carriers generated far from the heterojunction, which could be further improved by interfacial defects passivation and internal junction optimization.[28] The integrated J_{SC} calculated from EQE data is about 8.12 mA/cm^2 and is also comparable to the J-V measurement result.

4. Conclusions

In summary, Sb_2S_3-based thin films have been successfully prepared by magnetron sputtering combined with post-sulfurization or post-selenization heat treatment at different temperatures. The as-deposited thin film showed amorphous nature and then

the highly crystalline thin film composed of large crystal grains can be obtained after post heat treatment. Temperature-induced crystallization, preferential orientation, stoichiometric ratio variation and surface morphologies evolution also suggest it is crucial to control the post-sulfurization or post-selenization temperature to obtain high-quality thin film. Then Sb_2S_3 thin film solar cells with substrate structure of Mo/Sb_2S_3/CdS/ITO/Ag were fabricated. The device based on crystalline S-Sb_2S_3 thin film post-sulfurized at 450 °C can achieve a PCE of 0.49%. In contrast, an optimal device based on compact and uniform Se-Sb_2S_3 thin film post-selenized at 400 °C can achieve an interesting PCE of 0.95%, which is about two times higher. The corresponding EQE also showed an increased value and an extended region. Future work will be aimed at further investigating the thin film preparation process, improving the device performances through efficient interfacial defects passivation and internal junction optimization, and finally to obtain high efficiency substrate structured Sb_2S_3 thin film solar cells.

Acknowledgements

This work was supported by National Key R&D Program of China (No. 2018YFE0203400), The Key Project of Department of Education of Guangdong Province (No. 2018KZDXM059), National Natural Science Foundation of China (No. 61404086, 51604088), Shenzhen Key Lab Fund (ZDSYS 20170228105421966), Science and Technology plan project of Shenzhen (JCYJ20180305124340951) and Natural Science Foundation of SZU (Grant No. 85304/00000297, 827/000342).

References

[1] E. Kabir, P. Kumar, S. Kumar, A. A. Adelodun, K. H. Kim, Solar energy: Potential and future prospects. *Renewable Sustainable Energy Rev*. 2018, *82*, 894-900.

[2] R. Kondrotas, C. Chen, J. Tang, Sb_2S_3 Solar Cells. *Joule* 2018**,** *2*, 857-878.

[3] L. Zhang, Y. Li, C. Li, Q. Chen, Z. Zhen, X. Jiang, M. Zhong, F. Zhang, H. Zhu, Scalable Low-Band-Gap Sb_2Se_3 Thin-Film Photocathodes for Efficient Visible-Near-Infrared Solar Hydrogen Evolution. *ACS Nano* 2017, *11*, 12753-12763.

[4] H. Lei, J. Chen, Z. Tan, G. Fang, Review of Recent Progress in Antimony Chalcogenide - Based Solar Cells: Materials and Devices. *Solar RRL* 2019, 1900026.

[5] A. Polman, M. Knight, E. C. Garnett, B. Ehrler, W. C. Sinke, Photovoltaic materials: Present efficiencies and future challenges. *Science* 2016, *352*, aad4424.

[6] W. K. Metzger, S. Grover, D. Lu, E. Colegrove, J. Moseley, C. L. Perkins, X. Li, R. Mallick, W. Zhang, R. Malik, J. Kephart, C. S. Jiang, D. Kuciauskas, D. S. Albin, M. M. Al-Jassim, G. Xiong, M. Gloeckler, Exceeding 20% efficiency with in situ group V doping in polycrystalline CdTe solar cells. *Nat. Energy* 2019, *4*, 837–845.

[7] C. Yan, J. Huang, K. Sun, S. Johnston, Y. Zhang, H. Sun, A. Pu, M. He, F. Liu, K. Eder, L. Yang, J. M. Cairney, N. J. Ekins-Daukes, Z. Hameiri, J. A. Stride, S. Chen, M. A. Green, X. Hao, Cu_2ZnSnS_4 solar cells with over 10% power conversion efficiency enabled by heterojunction heat treatment. *Nat. Energy* 2018, *3*, 764-772.

[8] H. Deng, Y. Zeng, M. Ishaq, S. Yuan, H. Zhang, X. Yang, M. Hou, U. Farooq, J. Huang, K. Sun, R. Webster, H. Wu, Z. Chen, F. Yi, H. Song, X. Hao, J. Tang, Quasiepitaxy Strategy for Efficient Full-Inorganic Sb_2S_3 Solar Cells. *Adv. Funct. Mater.* 2019, *29*, 1901720.

[9] S. Chen, Z. Zheng, M. Cathelinaud, H. Ma, X. Qiao, Z. Su, P. Fan, G. Liang, X. Fan, X. Zhang, Magnetron sputtered Sb_2Se_3-based thin films towards high performance quasi-homojunction thin film solar cells. *Sol. Energy Mater. Sol. Cells* 2019, *203*, 110154.

[10] L. Yan, Q. Xue, M. Liu, Z. Zhu, J. Tian, Z. Li, Z. Chen, Z. Chen, H. Yan, H. L. Yip, Y. Cao, Interface Engineering for All-Inorganic $CsPbI_2$ Br Perovskite Solar Cells

with Efficiency over 14. *Adv. Mater.* 2018, 1802509.

[11] T. D. Lee, A. U. Ebong, A review of thin film solar cell technologies and challenges. *Renewable Sustainable Energy Rev.* 2017, *70*, 1286-1297.

[12] L. Zhang, C. Wu, W. Liu, S. Yang, M. Wang, T. Chen, C. Zhu, Sequential deposition route to efficient Sb_2S_3 solar cells. *J. Mater. Chem. A* 2018, *6*, 21320-21326.

[13] C. Jiang, R. Tang, X. Wang, H. Ju, G. Chen, T. Chen, Alkali Metals Doping for High-Performance Planar Heterojunction Sb_2S_3 Solar Cells. *Solar RRL* 2019, *3*. 1800272.

[14] T. Fukumoto, T. Moehl, Y. Niwa, Nazeeruddin, K. M. M. Grätzel, L. Etgar, Effect of Interfacial Engineering in Solid-State Nanostructured Sb_2S_3 Heterojunction Solar Cells. *Adv. Energy Mater.* 2013, *3*, 29-33.

[15] Y. C. Choi, D. U. Lee, J. H. Noh, E. K. Kim, S. I. Seok, Highly Improved Sb_2S_3 Sensitized-Inorganic-Organic Heterojunction Solar Cells and Quantification of Traps by Deep-Level Transient Spectroscopy. *Adv. Funct. Mater.* 2014, *24*, 3587-3592.

[16] S. Yuan, H. Deng, D. Dong, X. Yang, K. Qiao, C. Hu, H. Song, H. Song, Z. He, J. Tang, Efficient planar antimony sulfide thin film photovoltaics with large grain and preferential growth. *Sol. Energy Mater. Sol. Cells* 2016, *157*, 887-893.

[17] R. Tang, X. Wang, C. Jiang, S. Li, W. Liu, H. Ju, S. Yang, C. Zhu, T. Chen, n-Type Doping of Sb_2S_3 Light-Harvesting Films Enabling High-Efficiency Planar Heterojunction Solar Cells. *ACS Appl. Mater. Interfaces* 2018, *10*, 30314-30321.

[18] X. Wang, J. Li, W. Liu, S. Yang, C. Zhu, T. Chen, A fast chemical approach towards Sb_2S_3 film with a large grain size for high-performance planar heterojunction solar cells. *Nanoscale* 2017, *9*, 3386-3390.

[19] L. Zhang, D. Zhuang, M. Zhao, Q. Gong, L. Guo, L. Ouyang, R. Sun, Y. Wei, X. Lyu, X. Peng, Sb_2S_3 thin films prepared by vulcanizing evaporated metallic precursors. *Mater. Lett.* 2017, *208*, 58-61.

[20] G. Pan, D. Wang, S. Gao, P. Gao, Q. Sun, X. Liu, Z. Zhou, Y. Sun, Y. Zhang, Substrate structured Sb_2S_3 thin film solar cells fabricated by rapid thermal evaporation method. *Sol. Energy* 2019, *182*, 64-71.

[21] E. Zimmermann, T. Pfadler, J. Kalb, J. A. Dorman, D. Sommer, G. Hahn, J. Weickert, L. Schmidt-Mende, Toward High-Efficiency Solution-Processed Planar Heterojunction Sb_2S_3 Solar Cells. *Adv. Sci.* 2015, *2*, 1500059.

[22] X. Jin, Y. Yuan, C. Jiang, H. Ju, G. Jiang, W. Liu, C. Zhu, T. Chen, Solution processed NiO_x hole-transporting material for all-inorganic planar heterojunction Sb_2S_3 solar cells. *Sol. Energy Mater. Sol. Cells* 2018, *185*, 542-548.

[23] L. J. Zhang, C. H. Jiang, C. Y. Wu, H. X. Ju, G. S. Jiang, W. F. Liu, C. F. Zhu, T. Chen, V_2O_5 as Hole Transporting Material for Efficient All Inorganic Sb_2S_3 Solar Cells. *ACS Appl. Mater. Interfaces* 2018, *10*, 27098-27105.

[24] D. H. Kim, S. J. Lee, M. S. Park, J. K. Kang, J. H. Heo, S. H. Im, S. J. Sung, Highly reproducible planar Sb_2S_3-sensitized solar cells based on atomic layer deposition. *Nanoscale* 2014, *6*, 14549-54.

[25] W. Zhang, M. Tan, P. Zhang, L. Zhang, W. Dong, Q. Wang, J. Ma, E. Dong, S. Xu, G. Wang, One pot synthesis of Sb_2S_3 nanocrystalline films through a PVP-assisted hydrothermal process. *Appl. Surf. Sci.* 2018, *455*, 1063-1069.

[26] Y. Yin, C. Wu, R. Tang, C. Jiang, G. Jiang, W. Liu, T. Chen, C. Zhu, Composition engineering of Sb_2S_3 film enabling high performance solar cells. *Sci. Bull.* 2019, *64*, 136-141.

[27] C. Gao, J. Huang, H. Li, K. Sun, Y. Lai, M. Jia, L. Jiang, F. Liu, Fabrication of Sb_2S_3 thin films by sputtering and post-annealing for solar cells. *Ceram. Int.* 2019, *45*, 3044-3051.

[28] G. X. Liang, Z. H. Zheng, P. Fan, J. T. Luo, J. G. Hu, X. H. Zhang, H. L. Ma, B. Fan, Z. K. Luo, D. P. Zhang, Thermally induced structural evolution and performance of Sb_2Se_2 films and nanorods prepared by an easy sputtering method. *Sol. Energy Mater. Sol. Cells* 2018, *174*, 263-270.

[29] R. Tang, Z. H. Zheng, Z. H. Su, X. J. Li, Y. D. Wei, X. H. Zhang, Y. Q. Fu, J. T. Luo, P. Fan, G. X. Liang, Highly efficient and stable planar heterojunction solar cell based on sputtered and post-selenized Sb_2Se_3 thin film. *Nano Energy.* 2019, *64,* 103929.

[30] S. Qiao, J. Liu, Z. Li, S. Wang, G. Fu, Sb_2S_3 thickness-dependent lateral

photovoltaic effect and time response observed in glass/FTO/CdS/Sb_2S_3/Au structure. *Opt. Express* 2017, *25*, 19583.

[31] T. Kobayashi, T. Kumazawa, Z. Jehl Li Kao, T. Nakada, Cu(In,Ga)Se_2 thin film solar cells with a combined ALD-Zn(O,S) buffer and MOCVD-ZnO:B window layers. *Sol. Energy Mater. Sol. Cells* 2013, *119*, 129-133.

[32] D. J. Xue, S. C. Liu, C. M. Dai, S. Chen, C. He, L. Zhao, J. S. Hu, L. J. Wan, GeSe Thin-Film Solar Cells Fabricated by Self-Regulated Rapid Thermal Sublimation. *J. Am. Chem. Soc.* 2017**,** *139*, 958-965.

[33] W. Wang, X. Wang, G. Chen, L. Yao, X. Huang, T. Chen, C. Zhu, S. Chen, Z. Huang, Y. Zhang, Over 6% Certified $Sb_2(S,Se)_3$ Solar Cells Fabricated via In Situ Hydrothermal Growth and Postselenization. *Adv. Electronic Mater.* 2019, *5*, 1800683.

[34] S. Yuan, H. Deng, X. Yang, C. Hu, J. Khan, W. Ye, J. Tang, Postsurface selenization for high performance Sb_2S_3 planar thin film solar cells. *ACS Photonics* 2017, *4*, 2862-2870.

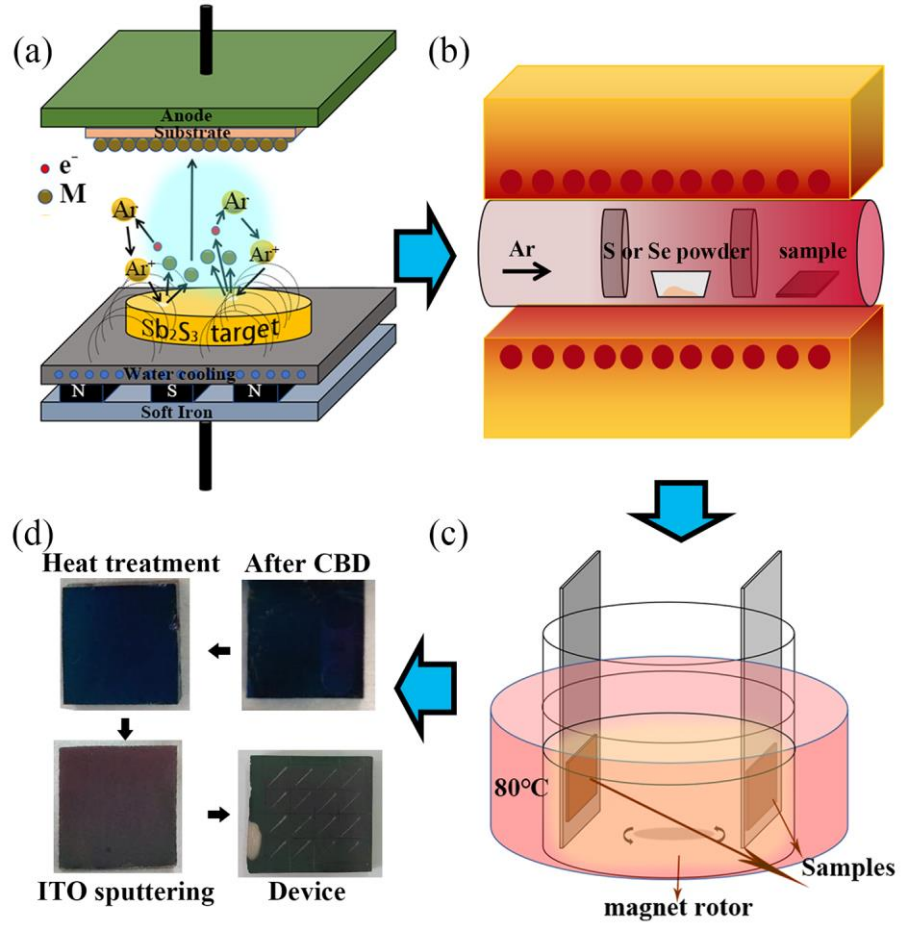

Fig. 1. Schematic illustration of the preparation process of the substrate structured Sb_2S_3 thin film solar cells. (a) Sb_2S_3 thin film deposition by RF magnetron sputtering, (b) Post-sulfurization or post-selenization heat treatment, (c) CdS buffer layer deposition via CBD method, (d) Representative photographs of the device.

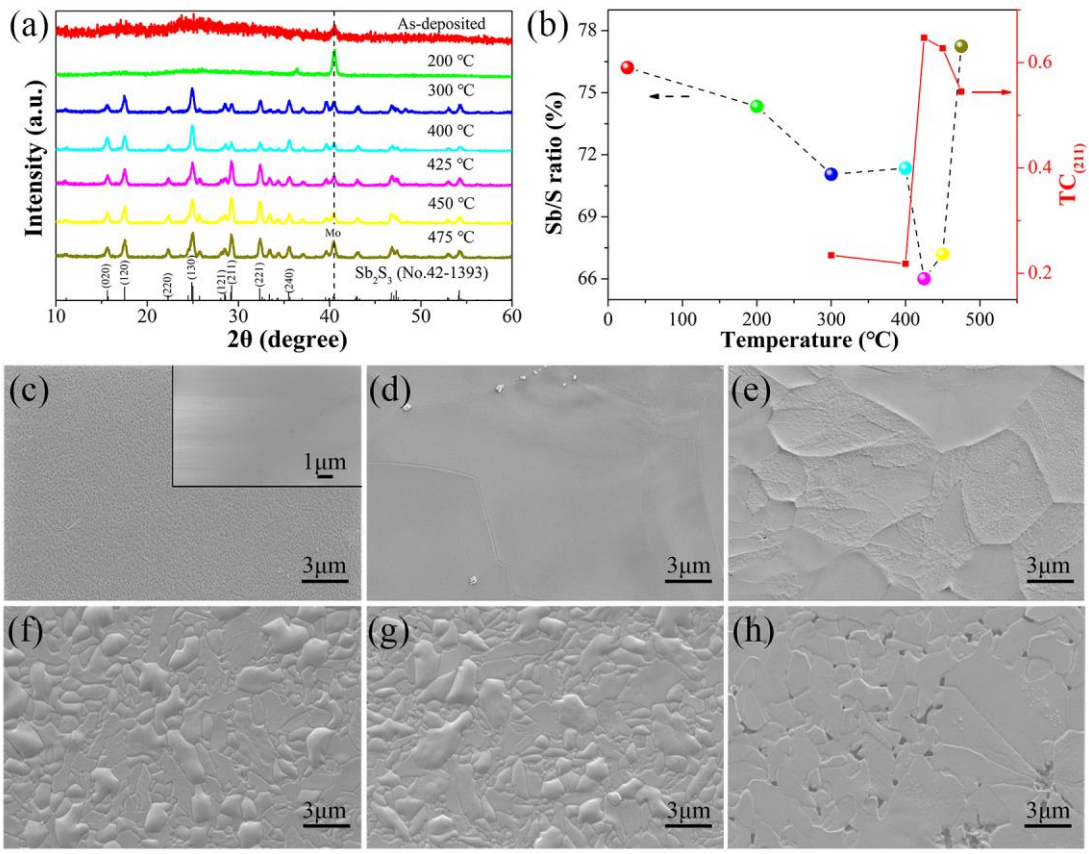

Fig. 2. Characterizations of the S-Sb_2S_3 thin films post-sulfurized at different temperatures: (a) XRD patterns, (b) Texture coefficients (TC) of (221) diffraction peaks based on XRD data and atomic ratio of Sb/S derived from EDS analysis. (c-h) Top-view morphologies of the thin films post-sulfurized at temperatures of (c) 200 ℃, the inset graph in (c) represents the as-deposited thin film, (d) 300 ℃, (e) 400 ℃, (f) 425 ℃, (g) 450 ℃ and (h) 475 ℃.

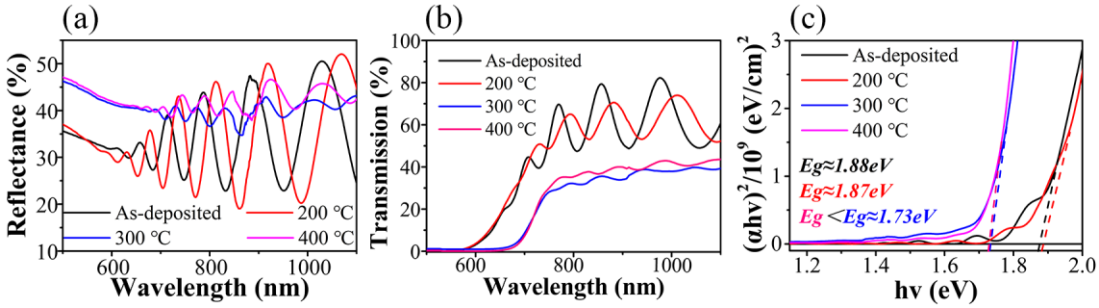

Fig. 3. Optical characterizations of the S-Sb_2S_3 thin films as a function of wavelength and with different post-sulfurization temperatures. (a) Reflection spectra, (b) Transmission spectra, (c) Plot of $(\alpha h\nu)^2$ versus hν, corresponding to direct band gap.

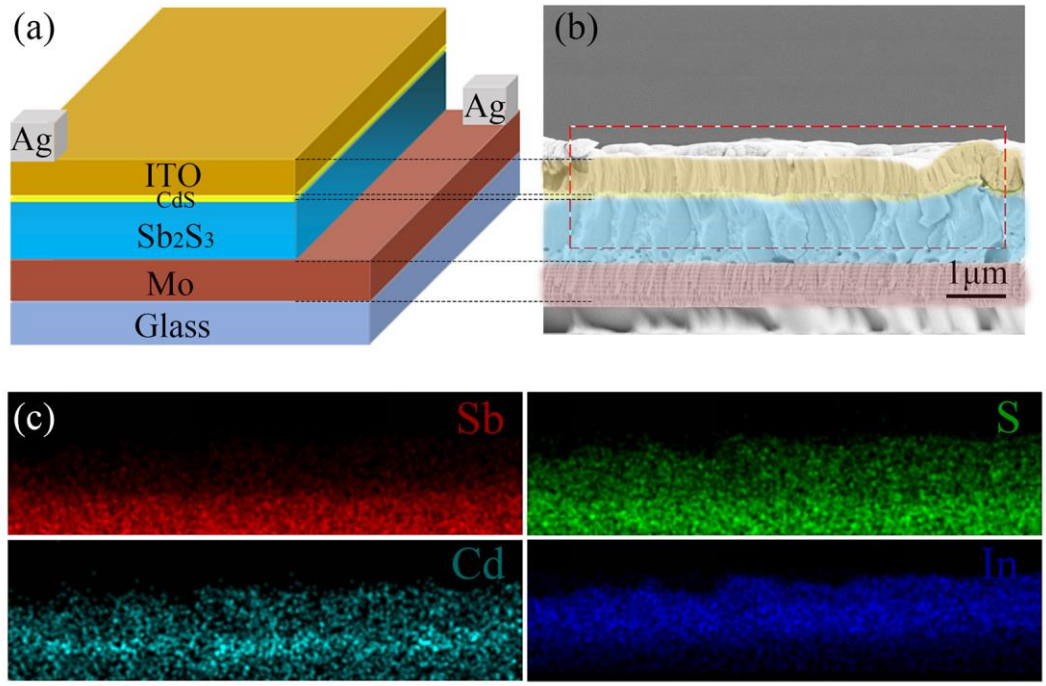

Fig. 4. (a) Schematic configuration of the substrate structured Sb_2S_3 thin film solar cell. (b) Cross-sectional SEM image of the device and (c) EDS elemental mappings derived from the dashed rectangle in (b) used to determine the compositional distribution.

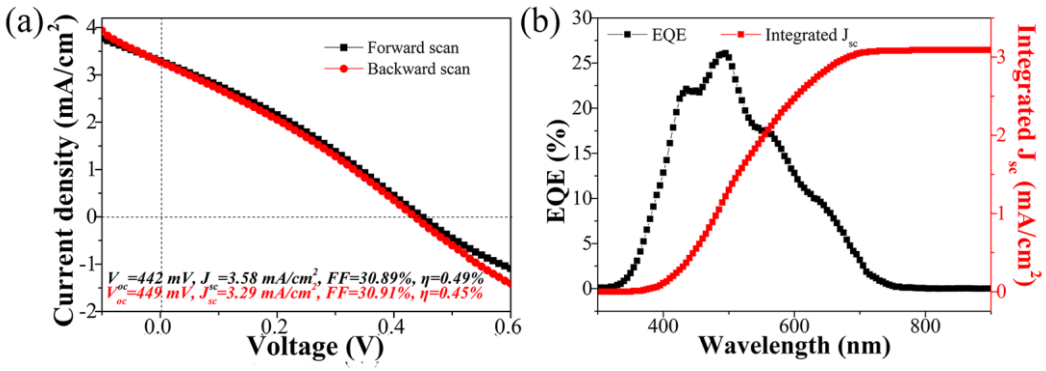

Fig. 5. J-V curves of the S-Sb_2S_3 thin film solar cell under forward scan and backward scan. (b) EQE and integrated J_{sc} of the device.

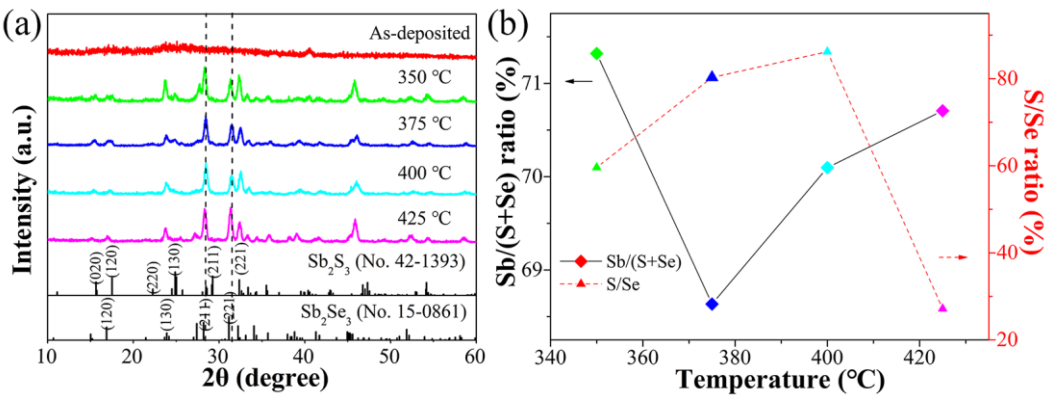

Fig. 6. (a) XRD patterns, (b) Atomic ratios of Sb/(S+Se) and S/Se derived from EDS analysis of the Se-Sb_2S_3 thin films with post-selenization at different temperatures.

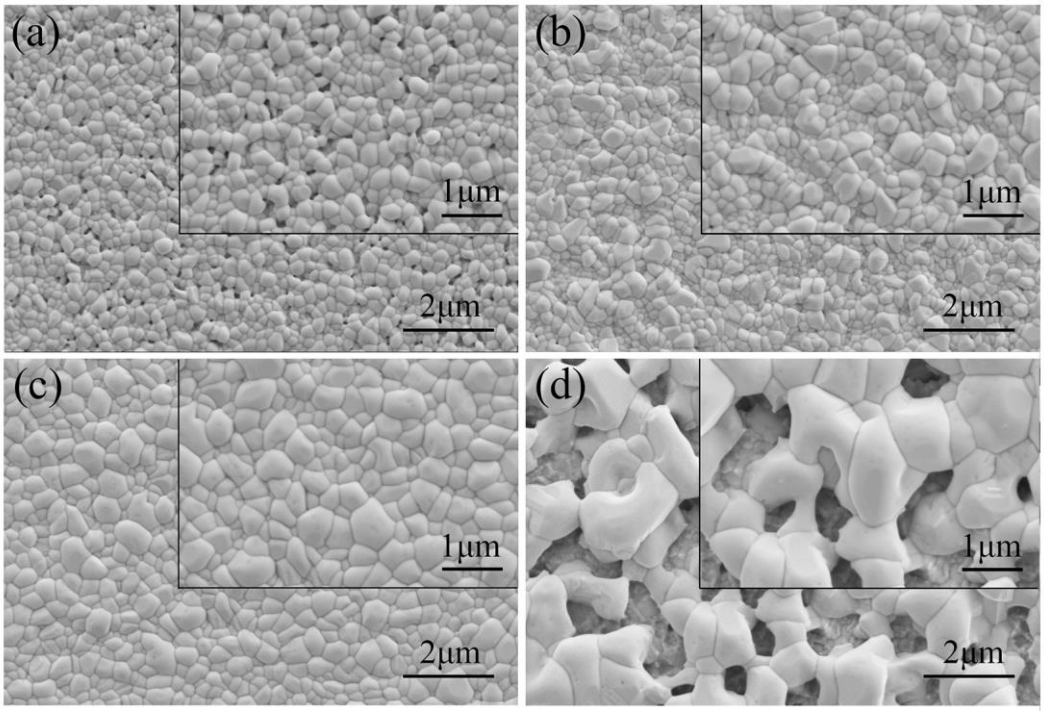

Fig. 7. Top-view morphologies of the Se-Sb_2S_3 thin films with post-selenization at temperatures of (a) 350 ℃, (b) 375 ℃, (c) 400 ℃ and (d) 425 ℃, the inset graphs are the corresponding magnified SEM images.

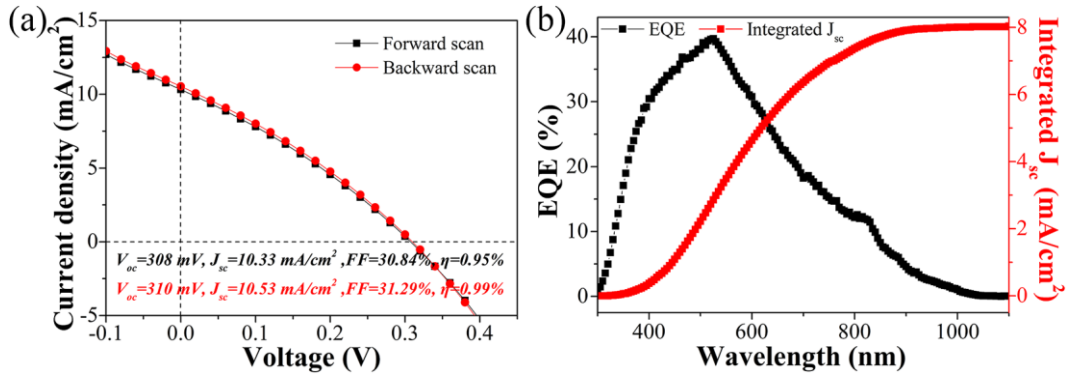

Fig. 8. J-V curves of the Se-Sb_2S_3 thin film solar cell under forward scan and backward scan. (b) EQE and integrated J_{sc} of the device.